

Suzaku Results on the Obscured Low-Luminosity Active Galactic Nucleus in NGC 4258

Shin'ya YAMADA,¹ Takeshi ITOH,¹ Kazuo MAKISHIMA,^{1,2} Kazuhiro NAKAZAWA,¹

¹ *Department of Physics, University of Tokyo*

7-3-1, Hongo, Bunkyo-ku, Tokyo, 113-0033, Japan

² *Cosmic Radiation Laboratory, Institute of Physical and Chemical Research (RIKEN)*

2-1 Hirosawa, Wako-shi, Saitama, 351-0198, Japan

yamada@amalthaea.phys.s.u-tokyo.ac.jp

(Received (reception date); accepted (accepted date))

Abstract

In 2006 June, the obscured low luminosity active galactic nucleus in the nearby Seyfert 1.9 galaxy NGC 4258 was observed with Suzaku for ~ 100 ks. Utilizing the XIS and the HXD, the nucleus emission was detected over a ~ 2 to ~ 40 keV range, with an unabsorbed 2–10 keV luminosity of $\sim 8 \times 10^{40}$ erg s $^{-1}$, and varied by a factor of ~ 2 during the observation. Its 2–40 keV spectrum is reproduced by a single power law with photon index of $\Gamma \sim 2.0$, absorbed by an equivalent hydrogen column of $\sim 1.0 \times 10^{23}$ cm 2 . The spectrum within 4' of the nucleus required also a softer thin-thermal emission, as well as an intermediate hardness component attributable to integrated point sources. A weak neutral Fe-K α fluorescence line was detected at an equivalent width of ~ 40 eV. The cold reflection component was not required by the data, with the reflector solid angle Ω seen from the nucleus constrained as $\Omega/2\pi \lesssim 0.3$ assuming a general case of 60° inclination. The results suggest that the cold reflecting material around the nucleus is localized along our line of sight, rather than forming a thick torus.

Key words: galaxies: active – galaxies: individual (NGC 4945) – galaxies: Seyfert – X-rays: galaxies

1. Introduction

Although active galactic nuclei (AGNs) exhibit a wide variety of spectral properties, a comprehensive classification of them, called “Unified Scheme” (e.g., Antonucci 1993), has been developed. In addition to the black hole mass and the mass accretion rate which are obvious parameters, this scheme employs two more fundamental parameters: radio loudness and our viewing direction to the accretion plane. A “type 1” AGN refers to an object with a nearly pole-on viewing angle, while a “type 2” AGN with a roughly edge-on aspect. The spectrum differs between the two classes depending on whether our line of sight is blocked by some part of the accreting material or not. The blocking material is often assumed to have a shape of an inflated torus around the nucleus, so called “molecular torus” or simply “torus”. This scheme can explain much of the observational differences among various kinds of AGNs. Nevertheless, the validity of the Unified Scheme and the nature of the putative torus are still open.

X-ray observations of type 2 AGNs provide a powerful tool in these attempts, because the strength of photoelectric absorption affecting the nuclear hard X-rays provides the most direct information on the column density of the obscuring material. Indeed, X-ray observations with Ginga (e.g., Koyama et al. 1989; Awaki et al. 1991), and ASCA (Ueno et al. 1996) of typical type 2 AGNs demonstrated that their nuclei are heavily obscured with a column density of 10^{23} to 10^{24} cm $^{-2}$. Subsequently, BeppoSAX investigators introduced a new concept called

“Compton thick AGNs” (Maiolino et al. 1998, Matt et al. 2000), as the most extreme class of type 2 AGNs, wherein the absorber is opaque not only to photoelectric absorption, but also to Compton scattering. Because of the strong suppression of the direct component, these objects are expected to provide further clues to the circumnuclear matter distribution, via detection of various secondary components, including in particular the Compton reflection hump, and fluorescent Fe-K lines.

Using Suzaku, we observed the Compton-thick AGN, NGC 4945, which is one of the brightest AGNs above 20 keV. Analyzing the data, Itoh et al. (2008) found the reflection features to be unusually weak, as judged from both the Fe-K edge feature in the XIS spectra and the Compton hump in the data from the HXD. Reinforced by the detection of clear hard X-ray variations, Itoh et al. (2008) thus constrained the reflection fraction $f_{\text{refl}} \equiv \Omega/2\pi$ to be less than a few percent, where Ω is the solid angle of the reflector as seen from the nucleus. This makes a significant contrast to many other Compton-thick Seyfert 2 AGNs, where we usually find $f_{\text{refl}} \sim 1$ –2 (e.g. De Rosa et al. 2008). Therefore, the reflector in NGC 4945 is suggested to have a geometrically-thin, disk-like structure rather than that of a thick torus, and the reflector, absorber, and the water maser source are thought to be provided by the same structure, namely a flat accretion disk (Madejski et al. 2000, 2006). Although this means a clear deviation from the Unified Scheme, it is not yet clear whether such a property is specific to NGC 4945, or more or less common to a certain class of AGNs. One of ef-

fective ways to examine this issue is to study AGNs with low mass-accretion rates, namely low luminosity AGNs (LLAGNs), because NGC 4945 has a rather low intrinsic (absorption corrected) luminosity as $\sim 1 \times 10^{43} \text{ erg s}^{-1}$ in 2–10 keV.

NGC 4258 (M 106), one of the typical LLAGNs, is a highly inclined (72° , Tully 1988) SABbc spiral galaxy located at a nearby distance of 7.2 Mpc (Herrnstein et al. 1999), where $1''$ corresponds to 35 pc. The presence of an obscured AGN was suggested by the strong polarization of the relatively broad optical emission lines (Wilkes et al. 1995), and H α and X-ray emitting “anomalous arms” (Cecil et al. 1995). The observation with ASCA up to 10 keV (Makishima et al. 1994) clearly demonstrated the presence of an LLAGN, absorbed by an equivalent hydrogen column of $N_H \sim 1.5 \times 10^{23} \text{ cm}^{-2}$, with an absorption-corrected 2–10 keV luminosity of $\sim 4 \times 10^{40} \text{ erg s}^{-1}$. The obscured nucleus was later reconfirmed by a Chandra image (Wilson et al. 2001; Yang et al. 2007). The epoch-making water maser observation (Miyoshi et al. 1995; Greenhill et al. 1995a; Greenhill et al. 1995b) established the AGN mass as $3.6 \times 10^7 M_\odot$, and its disk inclination as $\sim 83^\circ$. The X-ray flux is known to be variable on time scales of hours to years (Reynolds et al. 2000; Terashima et al. 2002; Fruscione et al. 2005; Fiore et al. 2001). According to observations with XMM-Newton (Pietsch and Read 2002) and Chandra (Yang et al. 2007), contributions by other softer X-ray components associated with NGC 4258 can be spectrally separated from the harder nuclear emission. Among them, the soft emission extending out from the nucleus, along “anomalous arms” is of particular interest, because of its possible association with the AGN jets (e.g., Wilson et al. 2001), but it is beyond the scope of the present paper.

The most outstanding property of the NGC 4258 nucleus is its extremely low luminosity, not only in the absolute sense but also relative to the Eddington value. Indeed, its absorption-corrected 2–10 keV luminosity is only $\sim 8 \times 10^{-6}$ of the Eddington value, which is much lower than those of Seyfert galaxies (typically thought to be of the order of $\sim 1\%$). Therefore, its accretion flow could be significantly different from those of Seyferts; e.g., the concept of Advection Dominated Accretion Flow (ADAF; Ichimaru 1977; Narayan and Yi 1994, 1995) may be more applicable to these LLAGNs than to Seyfert galaxies. Nevertheless, broad-band X-ray properties of NGC 4258 are not much different from those of radio-quiet Seyferts, as reported by Fiore et al. (2001) based on a BeppoSAX detection up to ~ 70 keV with a loosely constrained photon index of ~ 2.1 . Then, we may need to look for more subtle differences, e.g. in the reflection hump and Fe-K lines. Obviously, Suzaku is most suited for this purpose. In the present paper, we report on a tight upper limit on the reflection component in this LLAGN, and spectral changes on a time scale of ~ 50 ks, both derived from a Suzaku observation made in 2006 June.

2. Observation and Data Processing

2.1. Observation

During the AO-1 cycle, we observed NGC 4258 with Suzaku for a gross time span of 187.5 ks, from UT 12:49 on 2006 June 10 through UT 17:04 on June 12. The observation was carried out with the source placed at the center of the HXD field of view.

The XIS (Koyama et al. 2007) and the HXD (Takahashi et al. 2007; Kokubun et al. 2007) were operated both in the nominal modes throughout the observation. Event files from the two instruments were screened using version 2.2.7.18 of the Suzaku pipeline processing. We used “cleaned events” files, in which data of the following criteria were discarded: data taken with low data rate, or with an elevation angle less than 5° above dark Earth, or with elevation angles less than 20° above sunlit Earth, or during passages through or close to the South Atlantic Anomaly (SAA). Cut-off rigidity (COR) criteria of > 6 GV were applied to both the XIS and HXD data. In the present observation, the source was detected significantly with the XIS (section 2.2), and HXD-PIN (section 2.3), but not with HXD-GSO.

2.2. XIS Data Selection and Background Subtraction

XIS events with grades 0, 2, 3, 4 and 6 were selected, and then hot and flickering pixels in each CCD chip were removed using `cleansis` software. Using `aeattcor` software (Uchiyama et al. 2007), we corrected the event positions for attitude fluctuations due to thermal spacecraft wobbling. Then, we extracted those events which satisfy the criteria described in section 2.1. A net exposure of ~ 99 ks was obtained in total from each XIS sensor.

Figure 1 shows XIS0 images of the NGC 4258 region, in two energy ranges of 0.3–3 keV and 3–10 keV. The soft-band image is dominated by complex extended emission with an extent of at least $\sim 4'$, while the hard-band image is dominated by the bright nucleus as first revealed with ASCA (Makishima et al. 1994). In addition, several fainter point-like sources are distributed over the NGC 4258 disk. As indicated in figure 1, we accumulated XIS events from a circular region of radius $4'0$ (8.4 kpc at the distance of 7.2 Mpc) centered on the nucleus. Since the nuclear emission is confused in this region with the extended galaxy emission, we restrict the following spectral studies mainly to energies above 1.9 keV.

At $\sim 2'.2$ south of the nucleus, figure 2 reveals a faint point source which has not been reported previously. We excluded a circular region centered on the source, with a radius of $1'.0$ (indicated by a black dashed circle). Besides, the $4'$ -radius region for the nuclear signal accumulation contains a Chandra point source, J121857.3+471812 (Yang et al. 2007), located at $\sim 1''.5$ off the nucleus, of which the contribution is estimated to be $\sim 3\%$ at 3 keV and $\sim 1\%$ at 5 keV of the nucleus. We consider its contribution in section 3.1, together with those from other fainter point sources that can contaminate own spectra.

The background spectra were extracted from a source free region of the same field of view, as indicated by a

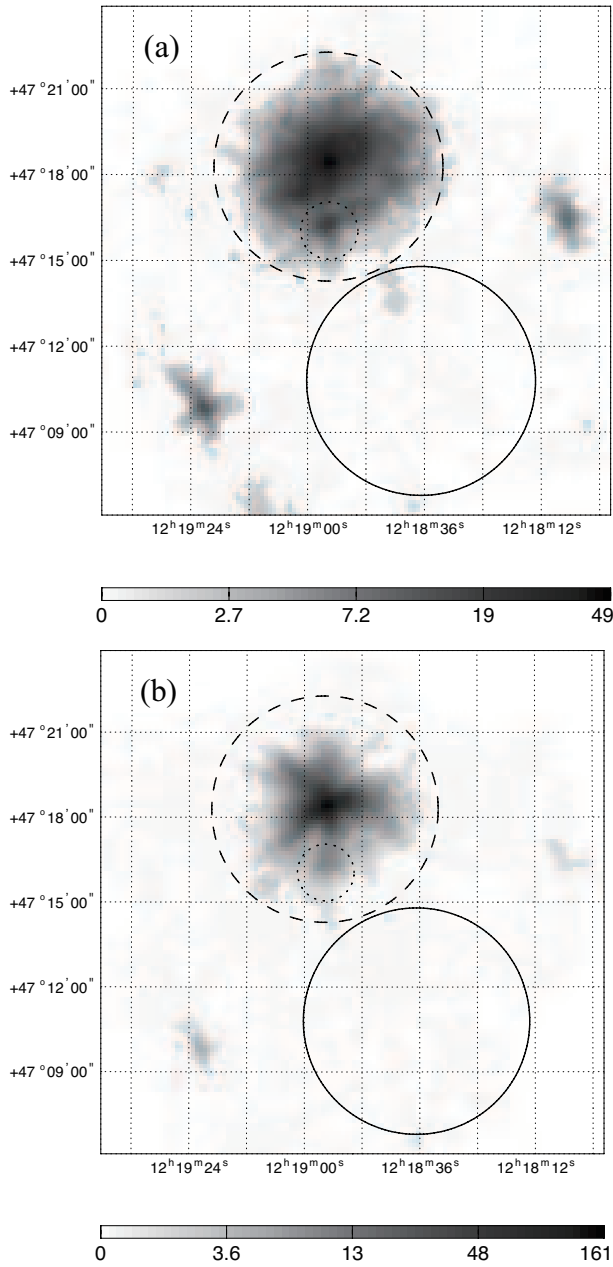


Fig. 1. Background-inclusive Suzaku XIS0 images of NGC 4258, in the 0.3–3.0 keV (panel a) and 3–10.0 keV (panel b) band. Dashed and solid circles, both of radius $4'$, indicate the on-source and background accumulation regions. A dotted small circle of radius $1'$ is a region used to eliminate a possible point source.

Table 1. The HXD count rates during the Earth occultation periods, compared with the NXB model.

Component	12–40 keV	40–60 keV
Earth event	0.4367 ± 0.0069	0.0492 ± 0.0023
NXB*	0.4504 ± 0.0021	0.0464 ± 0.0007
ratio	1.03 ± 0.02	0.94 ± 0.05

* Modeled with LCFITDT (Fukazawa et al. 2008).

black solid circle in figure 1. The background count rates in 3–9 keV were found to be $\sim 7\%$ of the total event rate in the same energy range detected with each FI CCD from the on-source region, and $\sim 10\%$ of those with the BI CCD. The response matrices and ancillary response files were created utilizing `xisrmfgen` and `xissimarfgen` (Ishisaki et al. 2007), respectively. In the spectral analysis described below, we coadded the spectra and responses of the three FI chips (XIS 0, 2, and 3).

2.3. HXD Data Selection and Background Subtraction

Table 1 summarizes the count rate of HXD-PIN averaged over the whole observation. To subtract the non X-ray background (NXB), we used an NXB model, called LCFITDT or “tuned” method (Fukazawa et al. 2008), which accurately takes into account various variations of the NXB. The model also includes slight differences caused by the different bias voltages imposed on the 64 HXD-PIN diodes. This is because a quarter of the whole HXD-PIN diodes have been operated with a bias voltage of 400 V since 2006 May 24 (to suppress anomalous noise behavior seen in some of the diodes) while the others were operated at 500 V. Systematic errors of the NXB model in 15–40 keV and 40–70 keV are estimated as 1.4% and 2.8% (1σ level), respectively, when night earth is observed for an exposure of 10 ks (Fukazawa et al. 2008). Since our observation is longer than 10 ks, the NXB model is expected to have a reproducibility no worse than these estimates. Therefore, we use these values as an approximation to the systematic errors involved in the NXB subtraction.

To further evaluate the systematic error of the NXB, we accumulated HXD-PIN spectrum while the satellite was pointing to the earth, with a exposure of 9.3 ks, and compared the results in figure 2 with the NXB model prediction. Thus, the modeled NXB spectrum is slightly higher than the Earth spectrum, especially around 12–20 keV. A more quantitative result of this comparison is given in table 1, where we find that the NXB is overestimated by $\sim 3\%$ in the 12–40 keV range, even though this is within the guaranteed accuracy of the present model (Fukazawa et al. 2008).

The counts remaining after subtracting the NXB still include the contribution of the cosmic X-ray background (CXB; Boldt 1987), which must be subtracted as well. The CXB contribution was estimated using the HXD-PIN response to diffuse sources, assuming the spectral CXB surface brightness model determined by HEAO 1 (Gruber

Table 2. Signal and background count rates from HXD-PIN during the on-source exposure.

Component	12-25 keV	25-40 keV	40-60 keV
On-source	0.3944 ± 0.0021	0.0925 ± 0.0010	0.0463 ± 0.0007
NXB*	0.3445 ± 0.0048	0.0832 ± 0.0004	0.0425 ± 0.0012
CXB†	0.0225	0.0040	0.0005
Net Signal‡	0.0274 ± 0.0022 ± 0.0048	0.0053 ± 0.0010 ± 0.0004	0.0035 ± 0.0007 ± 0.0012

* Modeled with LCFITDT (Fukazawa et al. 2008). The systematic errors are described in section 2.4.

† Predicted from the HEAO-1 measurement (Gruber et al. 1999).

‡ Net count rate obtained by subtracting the NXB and CXB from the on-source count rate. The first and the second uncertainties represent the statistical and systematic errors, respectively.

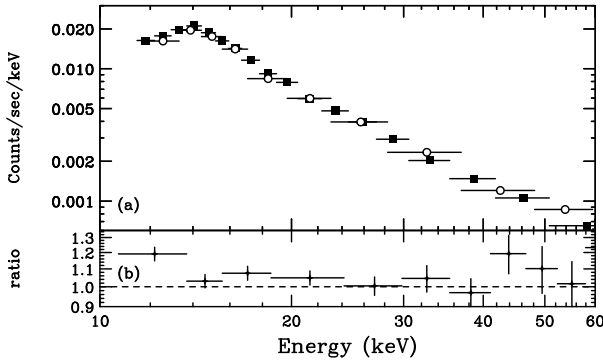


Fig. 2. (a) Raw HXD-PIN spectra (open circles) observed during the Earth-occultation periods, compared with the NXB model predictions (filled squares). (b) The model to data ratio.

et al. 1999): $9.0 \times 10^{-9} (E/3 \text{ keV})^{-0.29} \exp(-E/40 \text{ keV}) \text{ erg cm}^{-2} \text{ s}^{-1} \text{ str}^{-1} \text{ keV}^{-1}$, where E is the photon energy. The estimated CXB count rate is 5% of the NXB signals. The actual CXB normalization has recently been found (Revnivtsev et al. 2003; Churazov et al. 2007) to be higher by 10–15% at 10–100 keV than that of Gruber et al. (1999), but the difference is negligible because it is within the systematic uncertainty of the NXB subtraction. As indicated by table 2, the source has been detected significantly at least up to $\sim 40 \text{ keV}$ with a significance level of $> 5 \sigma$.

In contrast to the detections with HXD-PIN, the source was not detected with HXD-GSO. The estimated upper limit, $\sim 1 \text{ mCrab}$ at $\sim 50 \text{ keV}$, is consistent with an extrapolation from the HXD-PIN signals which indicate a source intensity of $\sim 0.6 \text{ mCrab}$ at 30 keV .

2.4. Light Curves

Figure 3 shows XIS-FI and HXD-PIN light curves of NGC 4258 from the present observation. In the 3–10 keV band, the source is gradually increasing and then decreasing by $\pm 10\%$ on time scales of $\sim 100 \text{ ks}$. In contrast, the light curves below 3 keV is much closer to being constant. These agree with the previous reports (e.g., Makishima et al. 1994) that the dominant emission in this energy range

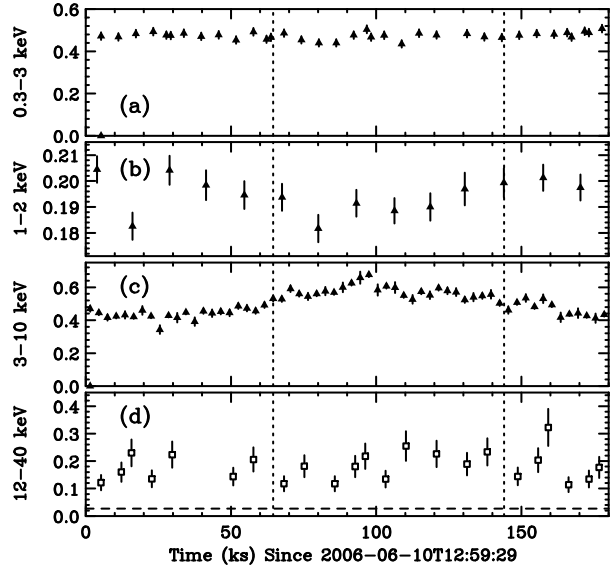


Fig. 3. Background-subtracted light curves of NGC 4258 taken with Suzaku. Panels (a), (b), (c), and (d) refer to those obtained with XIS-FI (0.3–3.0 keV), XIS-FI (1.0–2.0 keV), XIS-FI (3.0–10 keV), and HXD-PIN (12–40 keV), respectively. The bin widths in panels (a) through (d) are 2.5 ks, 10 ks, 3 ks, and 2.5 ks, respectively. The HXD-PIN result is presented after subtracting the NXB as described in section 2.2, and correcting for dead times. It includes the CXB contribution by 0.02 c s^{-1} (a dashed line in panel d). In contrast, the XIS light curves include NXB.

is thermal diffuse emission. Interestingly, some variations are suggested in the 1–2 keV band. Although the HXD-PIN light curve has rather poor photon statistics, it is inconsistent with being constant, because fitting it with a constant yields $\chi^2 \sim 79$ for 24 d.o.f.

2.5. Time-Averaged Spectra

Figure 4 shows time-averaged Suzaku spectra of NGC 4258. The HXD-PIN spectrum is corrected for the dead time, and is presented after subtracting the backgrounds (NXB + CXB) as described in section 2.2. As revealed with ASCA (Makishima et al. 1994) and BeppoSAX (Fiore et al. 2001), the XIS spectrum thus

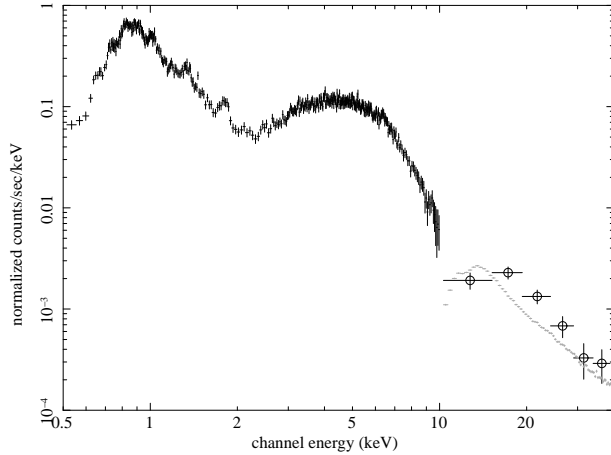


Fig. 4. Time-averaged XIS-FI (cross) and HXD-PIN (circle) spectra of the nuclear region of NGC 4258. The XIS spectrum is presented after subtracting the NXB, and the HXD-PIN data after subtracting the NXB + CXB. Both spectra are shown without removing the instrumental responses. For comparison, the 5% level of the modeled NXB of HXD-PIN is indicated in gray.

consists of at least two components, a soft thermal and the absorbed hard ones, dominant in energies below and above ~ 2 keV, respectively. To grasp overall features of the spectra, we divided them by those of the Crab Nebula, and show the results in figure 5. The ratio clearly reveals the two components mentioned above. However, the flux decrease from ~ 4 keV to ~ 2 keV is less steep than is described with a single-valued photoelectric absorption. It suggests that another component of a medium hardness (Makishima et al. 1994) extends up to ~ 3 keV. The Fe-K emission line is rather weak, and Fe-edge is not prominent.

Before conducting spectral fitting analysis, let us compare the spectra of NGC 4258 with those of NGC 4388, one of the typical Compton-thick AGNs. Specifically, we divided the Suzaku spectra of NGC 4388 (Shirai et al. 2008) by those of NGC 4258, and show the ratios in figure 6. The result reveals an intense Fe-K line and a prominent Fe-K edge, implying that these features are much stronger in NGC 4388 than in NGC 4258. Although the ratio increase from ~ 3 keV to ~ 10 keV is primarily understood as due to a heavier absorption in NGC 4388, the energy dependence is approximately power-law like. The statement would be reinforced if the possible contribution from a medium-hardness component in NGC 4258 is considered. This is presumably due to the strong reflection component in NGC 4388: conversely, we infer that the corresponding component is significantly weaker in NGC 4258. This inference is consistent with a slight decrease of the ratio from 20 keV to 30 keV, to be ascribed to the strong Compton reflection hump in NGC 4388 and its weakness in NGC 4258.

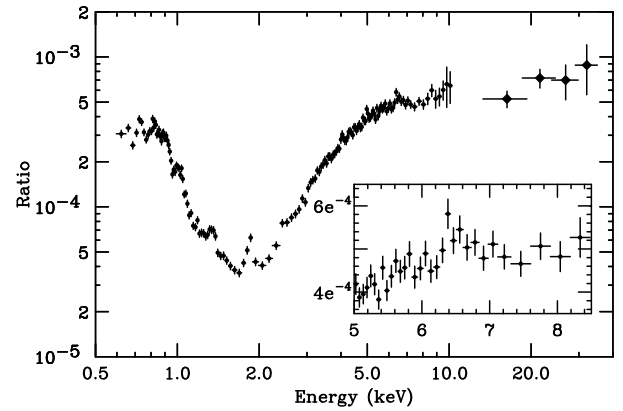


Fig. 5. The same spectrum as figure 3, normalized to those of the Crab Nebula acquired on 2005 September 15. The inset shows details around the Fe-K lines and edges.

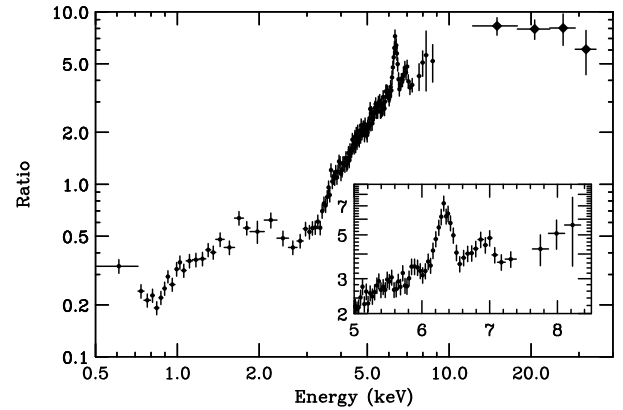


Fig. 6. Suzaku spectra of NGC 4388 (Shirai et al. 2008), divided by those of NGC 4258 presented in figure 4. The inset shows details around the Fe-K lines and edges.

3. Spectral Analysis

3.1. Analysis of the Time-Averaged 0.9–40 keV Spectra

To quantify the spectrum, we assign the PIN data points with a systematic error of 20%, which corresponds to an NXB uncertainty of $\sim 1.4\%$. At each spectral bin, this systematic error is added in quadrature to the statistical error. In the following spectral analysis we constrain each spectral model parameter to be the same among XIS-FI, XIS-BI, and HXD-PIN. The overall model normalization is set identical between XIS-FI and XIS-BI, while 13 % higher for HXD-PIN (Suzaku memo 2008-06). Furthermore, we ignore the 1.84–1.86 keV range due to the XIS response uncertainty around the Si edge.

Although our main interest is in the absorbed nuclear emission, its low-energy end ($\lesssim 4$ keV) is confused with other softer spectral components. To disentangle this effect, we start from a relatively wide energy range of 0.9–40 keV, discarding the softer ranges to avoid the complexity due to very soft components. Employing the procedure described above, we hence fitted simultaneously the XIS

(FI and BI) and HXD-PIN spectra, in the 0.9–9.0 keV, 0.9–8.0 keV, and 12.0–40 keV energy ranges, respectively. Figure 7a shows the case when we employed the simplest fitting model that consists of an absorbed power-law component and a single-temperature plasma emission model, representing the absorbed nuclear emission and the extended soft thermal emission, respectively. The plasma emission was modeled using *appec* code with a free temperature and a free overall metallicity (but keeping the solar abundance ratios), and was subjected to the Galactic absorption column of $1.2 \times 10^{20} \text{ cm}^{-2}$. The fit then gave, as the best estimates, a power-law photon index of $\Gamma \sim 1.93$, its absorbing column of $N_{\text{H}} \sim 1.1 \times 10^{23} \text{ cm}^{-2}$, and a plasma temperature and abundance of 0.58 keV and 0.47 solar, respectively. However, as evident in figure 7a, the fit was not acceptable, leaving significant residuals in the energy range of 1.5–2.5 keV where the two model components cross over. In addition, the fit residuals reveal a weak Fe-K line at ~ 6.4 keV.

As already mentioned in section 2.5 referring to figure 5, the 1.5–2.5 keV residuals indicate the presence of another spectral component with an intermediate hardness; Makishima et al. (1994) already noticed the same component, and attributed it to the integrated emission from point sources. Our results support this interpretation, because the very strong He-like Si K_{α} line (at 1.86 keV) and the weakness of its H-like counterpart (at 2.01 keV) imply that any hotter thin-thermal emission is unlikely to contribute significantly to our spectrum in energies above ~ 2 keV.

To improve the fit, we added a thermal bremsstrahlung model and a single Gaussian. The former is an empirical modeling of point sources (mostly thought to be low-mass X-ray binaries) after Makishima et al. (1994); we leave its temperature and normalization both free, and fix its absorption artificially at the value of $2 \times 10^{21} \text{ cm}^{-2}$ (Makishima et al. 1989) for a better approximation of integrated point-sources. The latter is allowed to have a free centroid and free intensity, but is assumed to be narrow ($\sigma = 0.001 \text{ eV}$). Then, as shown in figure 7b, the fit was significantly improved. As summarized in table 3, the temperature of the thermal bremsstrahlung was obtained with large errors as $kT_{\text{br}} = 11.1^{+19.1}_{-6.2} \text{ keV}$. This is because kT_{br} correlates negatively with the abundance of the thermal component, in such a way that a lower value of kT_{br} enhances its soft X-ray contribution, and hence reduces the continuum attributable to the plasma emission. If, e.g., the plasma abundance of the soft thermal component is fixed at 1.0 solar, we obtain $kT_{\text{br}} = 5.2^{+2.9}_{-3.0} \text{ keV}$, which is reasonable as a summed point-source spectrum from a spiral galaxy (Makishima et al. 1989). In addition, the 2.0–20 keV luminosity of this component, $5.8^{+2.9}_{-3.3} \times 10^{39} \text{ erg s}^{-1}$, is consistent with that interpretation (Makishima et al. 1989). We therefore choose the 1.0 solar abundance and $kT_{\text{br}} = 5.0 \text{ keV}$ as our baseline modeling. The model parameters obtained under these conditions are also given in table 3.

3.2. Time-Averaged Spectra above 1.7 keV

Although the above 4-component model is approximately successful, the fit is not yet fully acceptable; this would affect our error estimate. Since the fit residuals are seen in soft energies below ~ 2 keV, they are likely to be attributed to such effects as deviations of the plasma emission from the assumed isothermally and solar-ratio composition. Instead of trying to solve these issues, we decided to limit the fitting range to above 1.7 keV. The plasma abundance was again fixed at 1 solar, together with $kT_{\text{br}} = 5.0 \text{ keV}$. Then, the fit was significantly improved to $\chi^2/\nu = 518.4/449$. As summarized in table 3, the fit became still better, $\chi^2/\nu = 512.0/449$, by assigning a systematic error of 1% (Suzaku memo 2008-06) to the model.

As shown in figure 7c, we still observe a negative deviation around 12.0–25 keV in the HXD-PIN data, which could be due to the overestimated NXB in this energy range as noted in section 2.3 based on our Earth-occultation calibration. We therefore changed the NXB intensity to be subtracted by several percent from the nominal value, and repeated the fitting. Then, just as expected, the case of 2% reduced NXB made the fit acceptable with $\chi^2/\nu = 494.6/449$. As presented in figure 7d, the deviation around 12–40 keV apparently decreased. We therefore adopt this case as our best modeling, and summarize the parameters in table 3. Figure 8 shows the same spectra in the deconvolved $\nu F\nu$ form, where the deconvolution utilizes the best-fit model.

Under the above best-fit model, the nuclear emission has been modeled by an absorbed power law with a photon index of $\Gamma \sim 1.86$, absorbed by a column density of $N_{\text{H}} \sim 1.07 \times 10^{23} \text{ cm}^{-2}$. The temperature of the thermal plasma was determined as $\sim 0.76 \text{ keV}$, mainly by the intensity ratio between the He-like Si and H-like Si lines. The obtained unabsorbed 2.0–10.0 keV flux of the nuclear power-law component is $1.35 \times 10^{-11} \text{ erg cm}^{-2} \text{ s}^{-1}$, corresponding to a luminosity of $7.9 \times 10^{40} \text{ erg s}^{-1}$ at 7.2 Mpc. The narrow Gaussian emission line was obtained at $\sim 6.4 \text{ keV}$ with an equivalent width of $\sim 50 \text{ eV}$. In order to estimate the line width, we allowed the Gaussian to be broad, but this did not improve the fit significantly.

Although the data have already been reproduced successfully with this simple model, an AGN spectrum generally bears a feature due to “reflection” from circumnuclear cold materials. To evaluate its possible contribution to the NGC 4258 spectrum, we tentatively added a reflected continuum component (*pexrav* in XSPEC) to our fitting model. The input to *pexrav* was assumed to be a power-law with the same photon index as the intrinsic power-law, without a cutoff. The reflector was assumed to have solar abundances, and an inclination of $i = 60^\circ$ as a representative case. The inclusion of this additional component did not improve the fit, and its strength was constrained as $f_{\text{refl}} < 0.3$ at the 90 % confidence limit (the best-fit being at $f_{\text{refl}} = 0.063$ with $\chi^2/\nu = 494.5/448$). In order to understand how the data constrain f_{refl} , we repeated the fitting with f_{refl} purposely fixed at 1.0, sim-

Table 3. The best-fit parameters to the time-averaged Suzaku spectra, with 90 %-confidence error ranges.

Component	Parameter	0.9–40 keV		1.7–40 keV	
				NXB nominal	-2% NXB
PL	Γ	$1.93^{+0.05}_{-0.04}$	1.93 ± 0.01	1.88 ± 0.01	$1.86^{+0.01}_{-0.02}$
	N_{PL}^*	$4.62^{+0.01}_{-0.02}$	$4.75^{+0.67}_{-0.05}$	$4.21^{+0.01}_{-0.30}$	$4.22^{+0.01}_{-0.40}$
	N_{H}^\dagger	$11.1^{+0.3}_{-0.8}$	11.2 ± 0.2	$10.7^{+0.3}_{-0.2}$	$10.7^{+0.2}_{-0.2}$
Fe I $K\alpha$	E_{c}^\ddagger	$6.39^{+0.04}_{-0.03}$	$6.39^{+0.04}_{-0.03}$	$6.39^{+0.04}_{-0.03}$	$6.39^{+0.05}_{-0.04}$
	I^\S	$6.8^{+0.9}_{-1.4}$	$6.8^{+0.9}_{-1.9}$	$6.5^{+0.8}_{-2.4}$	$6.8^{+0.7}_{-2.5}$
	EW (eV)	$53.3^{+7.1}_{-11.0}$	$51.2^{+7.1}_{-14.3}$	$51.4^{+6.3}_{-19.0}$	$51.0^{+5.2}_{-18.8}$
bremss	kT_{br} (keV)	$11.1^{+19.1}_{-6.2}$	5 (fix)	5 (fix)	5 (fix)
	L^\parallel	4.9 ± 0.1	4.9 ± 0.1	$4.9^{+0.7}_{-1.5}$	$4.8^{+0.9}_{-1.4}$
apec	kT (keV)	0.58 ± 0.01	0.58 ± 0.01	$0.78^{+0.04}_{-0.05}$	$0.76^{+0.04}_{-0.05}$
	Abundance	$0.47^{+0.17}_{-0.13}$	1 (fix)	1 (fix)	1 (fix)
	L^\parallel	$4.3^{+24.5}_{-1.72}$	0.22 ± 0.03	0.36 ± 0.03	0.39 ± 0.03
Reflection	f_{refl}			< 0.3	< 0.3
$\chi^2/\text{d.o.f.}$		734.7/619	738.3/618	512.0/449	494.6/449

* The power-law normalization at 1 keV, in units of 10^{-3} photons $\text{keV}^{-1} \text{cm}^{-2} \text{s}^{-1}$ at 1 keV.

† Equivalent hydrogen column density in 10^{22}cm^{-2} .

‡ Center energy in keV.

§ Photon number flux in 10^{-6} photons $\text{cm}^{-2} \text{s}^{-1}$.

|| Integrated 2–20 keV luminosity at 7.2 Mpc in units of $10^{39} \text{erg s}^{-1}$.

ulating a reflector with an infinite slab geometry. Then, as shown in figure 7e, the HXD-PIN data became rather discrepant with the model, yielding $\chi^2/\nu = 527.4/449$. In other words, HXD-PIN would have to be measuring higher fluxes if the nuclear emission were accompanied by a reflection component with $f_{\text{refl}} \sim 1$. Thus, the HXD data play an essential role in constraining the reflection. To confirm that these results are not affected by the uncertainty in kT_{br} , we changed it to 2.0 keV and 10.0 keV, but both yielded $f_{\text{refl}} < 0.3$. For a further confirmation, we used the nominal NXB model instead of the 2% reduced one, but the upper limit on f_{refl} remained unchanged.

The above choice of $i = 60^\circ$ is considered appropriate for a general case, where reflecting materials assume a shape of an inflated torus as dictated by the Unified Scheme. However, the strong constraint on f_{refl} derived under this assumption suggests that the material is in reality localized in a limited solid angle containing our line of sight, like in the case of NGC 4945 (Itoh et al. 2008). To examine the consistency of this alternative configuration, we repeated the fitting assuming the reflector to have $i = 83^\circ$, which is the same as the inclination of the water-maser emitter (Miyoshi et al. 1995). Then, the constraint has been relaxed to $f_{\text{refl}} < 2.0$, and the case of $f_{\text{refl}} = 1.0$ (a flat infinite slab) became acceptable with $\chi^2 = 498.7$. In other words, the data are consistent with the presence of a slab-like reflector viewed nearly sideways. This result is reasonable, because signals from such a flat reflector will scale as $\sim \cos i$ in the observed spectra. Finally, we let i

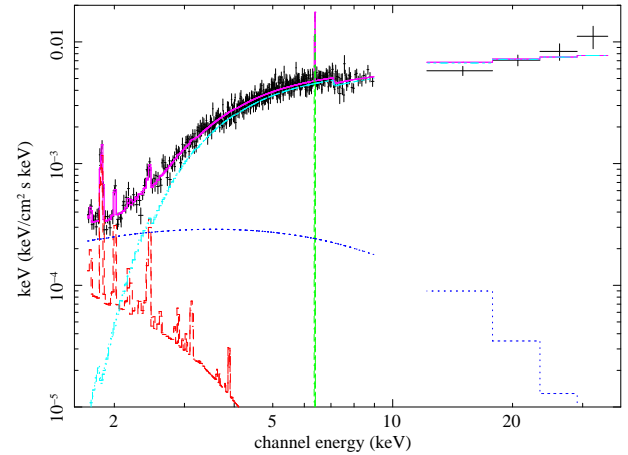


Fig. 8. The same spectra of NGC 4258 as in figure 7d, but presented in the deconvolved $\nu F\nu$ form. The observed data are shown in black, in comparison with the best-fit model in magenta. The thermal plasma, bremsstrahlung, narrow iron line, and the absorbed power-law components are shown in red, blue, green, and cyan, respectively.

and f_{refl} both float, and found that the data favor $i \sim 30^\circ$ but the fit does not improve ($\chi^2/\nu = 494.5/447$).

3.3. Analysis of Time Variations

During the present observation, the absorbed nuclear X-rays exhibited mild intensity variations (figure 3). In order to search the spectra for intensity-correlated changes,

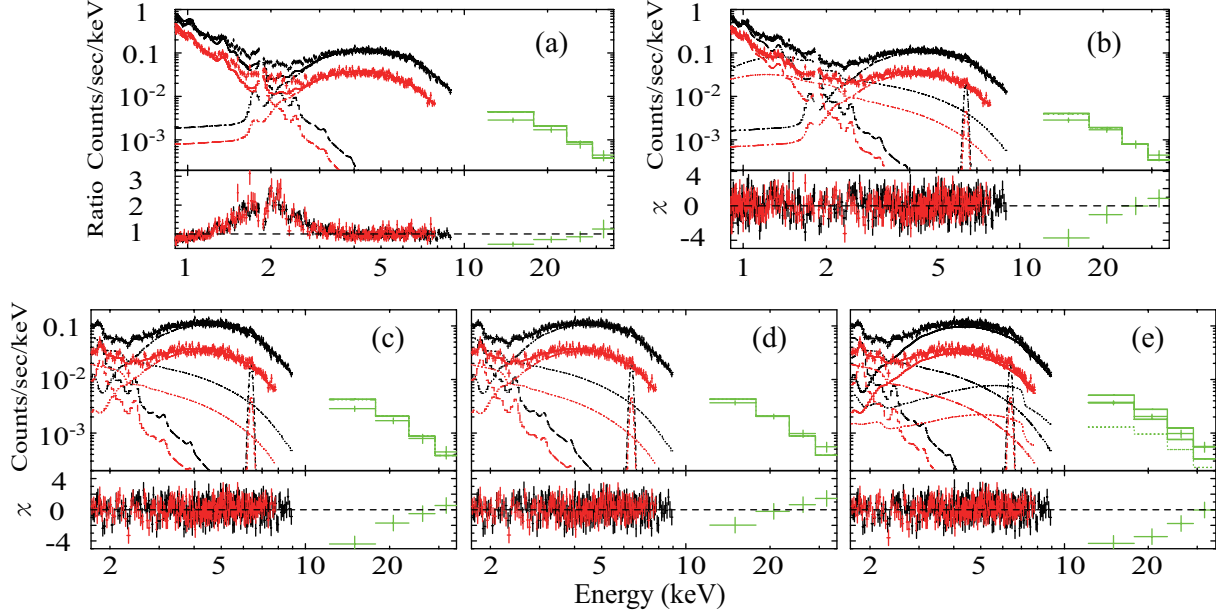


Fig. 7. Wide-band modeling of the background-subtracted XIS (black for FI and red for BI) and HXD-PI (green) spectra of NGC 4258. The employed energy range is 0.9–40.0 keV in panels (a) and (b), while 1.7–40 keV in panels (c), (d), and (e). (a) A fit with an absorbed power-law and a single temperature *apec* model. (b) An improved fit obtained by adding a bremsstrahlung component and a Gaussian. (c) A fit with the same model as panel (b), but using a narrower energy range. (d) The NXB level to be subtracted is reduced by 2%. (e) The same as panel (d), but a reflection component with $f_{\text{refl}} = 1.0$ is added.

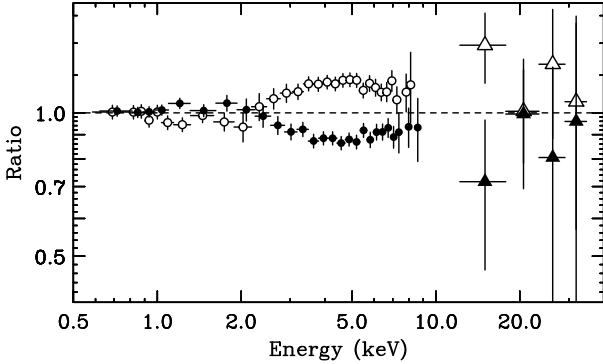


Fig. 9. Spectra from the “high-flux” (open) and “low-flux” (filled) phases, shown as their ratios to the time averaged spectrum. The XIS and PIN data points are shown in circles and triangles, respectively.

we divided the entire observation period into two subsets, namely “high-flux” and “low-flux” phases, when the 2–10 keV count rate is higher and lower than 0.5 cts s^{-1} , respectively. The two dotted lines in figure 3 separate them; the high-flux phase between the lines and the low-flux phase outside. The net exposure is 42.9 ks (XIS) and 38.7 ks (HXD) for the high-flux phase, and 57.0 ks (XIS) and 52.9 ks (HXD) for the low-flux phase.

Figure 9 shows the spectra from these two phases, divided by the time averaged spectrum. Thus, the variation is evident in energies above ~ 2.5 keV, in agreement with a simple idea that only the absorbed nucleus should vary. Interestingly, however, we observe small but significant variations in the 1.0–2.0 keV range, apparently in anti-

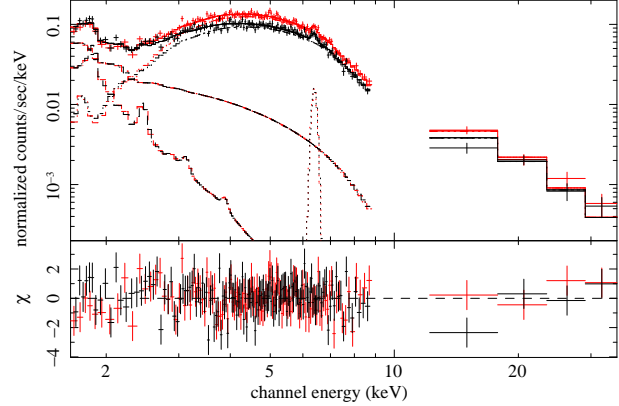


Fig. 10. The background subtracted spectra from the high-flux (red) and low-flux (black) phases, fitted with the same model as figure 7d. The XIS-BI spectrum, though employed in the fitting, is omitted from the plot for clarity.

phase with the dominant hard X-ray variations. This is also suggested by figure 3.

To quantify the intensity-correlated spectral changes, we fitted simultaneously the intensity-sorted spectra with the same model as employed in section 3.1. The normalization and temperature of the thermal plasma component was fixed to those obtained with the time averaged spectra, because such extended plasmas would not vary. Furthermore, we constrained the bremsstrahlung normalization and the Fe-K line flux to be the same between the two data sets. This is because the former is thought to be an assembly of many faint point sources, and the lat-

Table 4. The best-fit parameters to the high-flux and low-flux phase spectra over 1.7–40 keV of NGC 4258.*

Component	Parameter	High	Low	difference
Intrinsic PL	Γ	$1.96^{+0.03}_{-0.02}$	1.70 ± 0.02	$2.8^{+0.74}_{-0.61}$
	N_{PL}	$5.95^{+0.98}_{-0.07}$	2.73 ± 0.04	$7.5^{+23.5}_{-4.2}$
	N_{H}	11.3 ± 0.3	9.4 ± 0.3	$18.1^{+5.3}_{-4.2}$
Fe I K α	E_{c}	6.39 ± 0.05		
	I	$5.93^{+1.45}_{-1.35}$		
bremss	kT (keV)	5.0 (fix)		
	L	$4.3^{+0.3}_{-0.25}$		
apec	kT (keV)	0.76 (fix)		
	Abundance	1.0 (fix)		
	L	0.39 (fix)		
$\chi^2/\text{d.o.f.}$		435.8/436		45.2/42

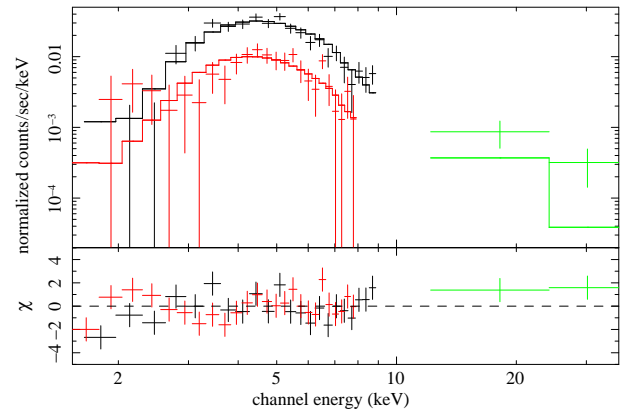
All physical quantities and their units are the same as in table 3.

ter is considered to arise at too large distances to vary significantly on ~ 100 ks. We retained the constraint of $kT_{\text{br}} = 5$ keV. The results became fully acceptable with $\chi^2/\nu = 435.8/436$, as presented in table 4 and figure 10. Thus, the nuclear emission became softer by $\Delta\Gamma \sim 0.3$ as the intensity increased, with a marginal evidence of an increase in N_{H} . This spectral steepening is most clearly visible in figure 9 over the 5–9 keV range of the XIS data. As a cross confirmation, we tentatively constrained Γ to be the same between the two data sets, to find that the fit worsens by $\Delta\chi^2 = 29.8$. The fit degradation is smaller ($\Delta\chi^2 = 6.5$) when we tie N_{H} instead of Γ .

In figure 3 and figure 9, the 1–2 keV signals exhibit a hint of weak variation. To examine this effect, we tentatively allowed the bremsstrahlung normalization to take separate values between the two phases, while keeping kT_{br} the same between them. Then, the bremsstrahlung normalization became $\sim 10\%$ lower in the high-flux phase than in the other, with a fit improvement by $\Delta\chi^2 = -4.6$ for $\Delta\nu = -1$. The 2–20 keV bremsstrahlung luminosity was obtained as 3.9 ± 0.4 and 4.5 ± 0.4 in the high-flux and low-flux phases, respectively, both in units of 10^{39} erg s $^{-1}$. Therefore, the small (anti-phased) variation seen in the 1–2 keV band of figure 3 is consistent with changes in the medium-hardness component. Further examination of this issue is presented in section 4.

The Fe-K line photon flux, when allowed to differ between the two phases, was obtained as 5.83 ± 2.35 and 5.95 ± 1.82 in units of 10^{-6} ph s $^{-1}$ cm $^{-2}$, during the high-flux and low-flux phases, respectively, together with $\Delta\chi^2 = -0.01$ ($\Delta\nu = -1$). Therefore, our assumption of a constant Fe-K photon flux is self-consistent. To examine an alternative case of constant EW, we next constrained the Fe-K line flux in the low-flux phase to be 0.8 times that in the high-flux phase, so that it becomes proportional to the continuum at 6.4 keV (figure 9). Then, the fit became rather worse by $\Delta\chi^2 = 2.7$. Thus, the constant-line-flux hypothesis is more favored than the constant-EW alternative, though not conclusive.

Figure 11 shows “difference spectra”, obtained by sub-

**Fig. 11.** The difference spectra taken with XIS-FI and HXD-PIN, fitted simultaneously by an absorbed single power-law. The color specification is the same as in figure 7.

tracting the low-flux phase data from those in the high-flux phase. As shown in table 4 (last column), the results can be described, in energies above 1.7 keV, by a rather steep power-law with $\Gamma \sim 2.8$. This reinforces the spectral softening in the high phase. However, the value of N_{H} required by the difference spectra is considerably higher than indicated by the time-averaged spectrum. Actually, when N_{H} is fixed at the value (1.1×10^{23} cm $^{-2}$) derived with the time-averaged spectrum, Γ becomes 1.8 ± 0.2 , but the fit worsens by $\Delta\chi^2 = 10.0$. While this could partially be due to a real increase in N_{H} toward higher fluxes as suggested by table 4, an artifact could also be working: by subtracting a flatter/weaker power-law from a steeper/stronger one, we will obtain a concave-shaped difference spectrum, and its approximation by a single power-law would require an artificially increased absorption.

4. Discussion

4.1. Summary of the results

In 2006 June, we observed NGC 4258 for ~ 100 ks with Suzaku. In addition to the soft thermal plasma emission, and a medium-hardness component presumably due to point sources, the absorbed hard emission from its LLAGN was detected with the XIS and HXD-PIN over a ~ 2 keV to ~ 40 keV band altogether. The acquired wide-band spectra of the nucleus have been described successfully in terms of a power-law with $\Gamma = 1.88$, absorbed by $N_{\text{H}} = 1.1 \times 10^{23} \text{ cm}^{-2}$. The absorption-corrected 2–10 keV luminosity of the nucleus, estimated as $\sim 8 \times 10^{40} \text{ erg s}^{-1}$, is typical of this LLAGN (e.g., Makishima et al. 1994, Reynolds et al. 2000, Pietsch et al. 2002, Yang et al. 2007). A narrow Fe-K line at 6.4 keV was detected at a relatively low EW of ~ 50 eV. The reflection component was insignificant, with an upper limit of $f_{\text{refl}} < 0.3$ if the reflector is assumed to have $i = 60^\circ$, although it is relaxed to $f_{\text{refl}} < 2.0$ if the water-maser configuration of $i = 83^\circ$ is adopted (Miyoshi et al. 1995).

On a time scale of ~ 100 ks, we detected a clear hard X-ray variation by 20%, which can be explained by a change in the nuclear component. As the hard X-ray flux increased, the power-law component steepened by $\Delta\Gamma \sim 0.3$ with marginal evidence for an increase in N_{H} . The varying component was described by a relatively steep power-law with $\Gamma \sim 2.8$.

4.2. Implications of the time-averaged spectrum

Being a prototypical LLAGN, the most outstanding feature of the NGC 4258 nucleus is of no doubt its very low X-ray luminosity, both in the absolute and relative sense. Hence, one of the most intriguing questions is whether it exhibits any X-ray signatures (other than its low luminosity) that are considered specific to LLAGNs. When trying to answer this question, the wide-band spectral coverage of Suzaku, with its good energy resolution, is considered essential. As part of such attempts, we may quote X-ray photon indices of the intrinsic nuclear component of several representative Seyferts, determined with Suzaku through careful separation of the reflection component. The results include $\Gamma \sim 1.6$ in NGC 4945 (Itoh et al. 2008), $\Gamma \sim 1.7$ in NGC 4388 (Shirai et al. 2008), $\Gamma \sim 1.8$ in MCG 5–23–16 (Reeves et al. 2007), and $\Gamma \sim 1.9$ in NGC 3516 (Markowitz et al. 2008). Thus, our results on NGC 4258, $\Gamma \sim 1.9$, does not distinguish this LLAGN from the other Seyferts.

Then, what do we find about circum-nuclear matter distribution in NGC 4258? Generally, this can be probed using reprocessed signals, including in particular the fluorescence iron lines and the reflection component. The measured EW (~ 50 eV) of the former component, which agrees with previous measurements from this LLAGN (Makishima et al. 1994; Fiore et al. 2001), is significantly smaller than those generally found among Seyfert galaxies of both type 1 (typically ~ 150 eV) and type 2 (up to ~ 1 keV; Ueda et al. (2007)). The latter component, i.e. reflection, consists of three spectral features; a deep Fe-K

edge at ~ 7 keV, a Compton hump above 10 keV, and a hard continuum approximated by $\Gamma \sim -0.3$ (rising with the energy; figure 7e) below the Fe-K edge. While the last feature is confused in our spectrum with the point-source contribution, the iron edge is clearly very weak (figures 5 and 6). Furthermore, the HXD-PIN data, combined with the XIS flux points, rule out the presence of a strong Compton hump. Assuming a general configuration of $i = 60^\circ$, we have thus obtained a tight constraint as $f_{\text{refl}} < 0.3$, which falls much below those typically found with Seyferts ($f_{\text{refl}} \sim 1 - 2$; De Rosa et al. 2008).

The above results on the Fe-K line and reflection both means that the nucleus of NGC 4258 is devoid of thick materials with large solid angles. As a result, an inflated torus (for which $i = 60^\circ$ is regarded as a reasonable approximation) is unlikely to be present around it. Nevertheless, our direct view to the nucleus is obscured by a thick material with $N_{\text{H}} \sim 1 \times 10^{23} \text{ cm}^{-2}$. Then, the obscuring material must be localized to a limited solid angle including our line of sight, rather than forming a thick torus. In fact, our data are consistent with a slab-like matter distribution with $f_{\text{refl}} \sim 1$, as long as it is viewed from an edge-on direction (section 3.2). One likely scenario is that the nearly edge-on and warped accretion disk, which has been revealed by the water-maser results, causes a grazing obscuration of the nucleus.

After NGC 4945 (Itoh et al. 2008), the NGC 4258 nucleus thus becomes a second example in which the circum-nuclear matter is inferred to have a thin disk geometry rather than a thick toroidal shape. While such objects are obviously considered relatively rare in a statistical sense, we must investigate the reason why these objects lack a thick torus that is usually considered to be a common attribute of an AGN. The 2–10 keV luminosity of $8 \times 10^{40} \text{ erg s}^{-1}$, measured from NGC 4258, translates to a bolometric luminosity of $L_{\text{bol}} \sim 6 \times 10^{41}$, if we use the argument by Marconi et al. (2004), assuming that the multi-wavelength spectra of LLAGNs are not much different from those of typical AGNs. The estimated L_{bol} is still only $\sim 1 \times 10^{-4}$ of the Eddington limit for an object of $3.6 \times 10^7 M_{\odot}$. In contrast, the Eddington-normalized bolometric luminosity of NGC 4945 amounts to 0.3–1.0 (Itoh et al. 2008). Therefore, a low *normalized* luminosity is unlikely to provide a common account for the lack of a torus.

When we consider the absolute luminosity (or mass accretion rate) instead of the normalized one, not only NGC 4258 but also NGC 4945 has a considerably lower value ($7 \times 10^{42} \text{ erg s}^{-1}$ in 2–10 keV after correcting for the absorption and Compton scattering; Itoh et al. 2008) than typical AGNs (e.g., $10^{43-44} \text{ erg s}^{-1}$; Tueller et al. 2008): the high normalized luminosity of NGC 4945 is simply a results of its low black-hole mass ($1.4 \times 10^6 M_{\odot}$; Greenhill et al. 1997). Thus, a common feature of the two objects is very low accretion rates. We hence speculate that the presence/absence of a thick torus is related to the mass accretion rate rather than to the normalized luminosity. Considering causality, one possible scenario is that a high accretion rate onto a giant black hole at the galaxy nucleus is realized when the matter distribution

has (for some unspecified reasons) an inflated toroidal geometry, whereas the rate remains low when the matter has a thin disk configuration.

An accretion flow under an extremely low rate, like in the present case, may be described by the ADAF model (Narayan et al. 1995), which assumes the optically-thick accretion disk to be truncated at a large radius. Lasota et al. (1996) applied the ADAF prediction to the X-ray spectrum of NGC 4258 measured by Makishima et al. (1994), and argued that the innermost radius of the accretion disk, r_{in} , should be larger than $\sim 100 r_g$ in this LLAGN, where r_g is the Schwarzschild radius ($= GM/c^2$). Since our spectrum is basically similar to that measured by Makishima et al. (1994), the result by Lasota et al. (1996) may also be applicable to our case. Such a condition is consistent with our data, because they also allow a solution with $i = 82^\circ$ and $f_{\text{refl}} \sim 0$. Incidentally, Makishima et al. (2008) measured $f_{\text{refl}} \sim 0.4$ from Cygnus X-1, together with $r_{\text{in}} \sim 15 r_g$. Therefore, the concept of ADAF may be more applicable to NGC 4258 than to Cygnus X-1.

4.3. The time variations

The time variation we detected, on a time scale of ~ 100 ks, is one of the most rapid changes ever observed from NGC 4258. We discovered that the power-law spectrum softens by $\Delta\Gamma \sim 0.3$ when the nucleus brightens up by 20%. This result is apparently reminiscent of the positive correlation between Γ and flux, measured repeatedly from other AGNs; e.g., from NGC 4151 with EXOSAT and Ginga (Warwick et al. 1989; Yaqoob et al. 1992), and from NGC 4051 with ASCA (Guainazzi et al. 1996). Such positive Γ vs. flux correlations allow two alternative interpretations. One is to assume that this is an intrinsic property of the nuclear emission, possibly related to cooling of hot electron “coronae” that produce hard X-rays via thermal Comptonization of some soft seed photons (e.g., Sunyaev & Trümper 1979). The other is to consider the relation as an artifact, produced by a superposition of a power-law component which varies without changing its slope, and a constant (and harder) reflection component.

As to black hole binaries in so-called Low-Hard state, including Cygnus X-1 in particular, Suzaku observations (Makishima et al. 2008) revealed that the former is actually occurring at least on time scales longer than 1 s. (The latter mechanism does not work on this time scale, since the reflection catches up with the intrinsic nucleus variation). In the case of AGNs, in contrast, the latter is likely to be dominant, because their “difference” spectra can be generally expressed by a single power-law, of which the photon index is close to what is found with the time-averaged spectrum after separating the reflection component. Such examples include NGC 4945 (Itoh et al. 2008) and MCG 5–23–16 (Reeves et al. 2007). Returning to NGC 4258, our results prefer the former interpretation, because the reflection component is basically insignificant in this object. Then, the mechanism responsible for the variation of this LLAGN is suggested to be closer to that of black-hole binaries in the Low-Hard state than to those

of Seyfert galaxies.

An intriguing result is the weak variation in the 1–2 keV band, apparently anti-correlated with that in the absorbed power-law. One possible interpretation is to invoke a variation of a small number of luminous point sources, as suggested by the analysis conducted in section 3.3. However, the implied luminosity change amounts to $\sim 5 \times 10^{38} \text{ erg s}^{-1}$, which would be too large to be explained by such a mechanism. Furthermore, we would have to invoke a chance coincidence to explain the apparent anti-correlation between the 1–2 keV and hard-band variations. Therefore, it is more natural to consider that the soft-band signals are contributed not only by point sources, but also by the nucleus at some level, and the variation therein is attributable to the nucleus contribution. Since the absorbed power-law component falls far below ($\sim 1/30$) the overall signal intensity at 1.5 keV (figure 8), this interpretation requires that a small (e.g., $\sim 1\%$) fraction of the intrinsic emission reaches us without being absorbed. Below, we construct a possible explanation based on this idea.

Let us recall that the hard X-rays from Seyfert-like objects are likely to be emitted from a hot corona with a relatively large scale height, via Compton scattering by thermal electrons (Makishima et al. 2008). If such a corona is viewed from sideways, its line-integrated Compton emissivity is expected to decrease rapidly as a height away from the accretion plane (like in the limb regions of solar coronae). Then, the highest part of the corona, which carries only a small fraction of the overall emissivity (but geometrically rather extended), could be rising above the grazing absorber and hence directly visible. If the height of this corona is time variable, the hard X-ray intensity will increase when the corona becomes less tall, because the Compton optical depth of the corona will increase due to compression. At the same time, the directly-visible fraction of the coronal top region will decrease, and will reduce the unabsorbed X-ray flux. Furthermore, the absorber may have a gradient in the column density, in such a way that it decreases away from the accretion plane. Then, a more compressed corona will sample on average lower heights of the absorber, leading to a slight enhancement in N_{H} as suggested by the data (table 4).

As a consistency check of the above scenario, a typical scale of such a corona is estimated as several tens r_g if an analogy to Cygnus X-1 is adopted (Makishima et al. 2008). In the present case of NGC 4258, such a corona can vary just on ~ 50 ks, assuming a Keplerian time scale at such radii. Furthermore, the Comptonizing corona of Cygnus X-1 was revealed to be highly inhomogeneous (Makishima et al. 2008), and its hard X-ray intensity was suggested to increase when the corona becomes “less porous”. This is consistent with the height variation we invoked above, because an inhomogeneous corona will naturally become less porous when it becomes vertically shorter. For a final speculation, a corona may become vertically shorter and less porous (thus leading to an increased hard X-ray intensity), as its internal magnetic pressure is released by magnetic reconnection.

The authors would like to express their thanks to the Suzaku team members. Our work was supported by Grant-in-Aid for JSPS Fellow.

References

- Antonucci, 1993, *ARA&A*, 31, 473
 Awaki, H., Kunieda, H., Tawara, Y., Koyama, K., 1991, *PASJ*, 43, 195-212
 Boldt, E. 1987, *Phys. Rep.*, 146, 215
 Cecil, G., Morse, Jon A., Veilleux, S., *ApJ*, 452, 613-626
 Churazov, E., et al. 2007, *A&A*, 467, 529
 A. De Rosa, A., Bassani, L., Ubertini, P., Panessa, F., Malizia, A., Dean, A. J., Walter, R. 2007, *A&A*, 483, 749-758
 Fukazawa, Y. et al., 2008, *PASJ in prep*
 Fiore, F. et al., 2001, *ApJ* 556, 150
 Fruscione, A., Greenhill, L. J., Filippenko, A. V., Moran, J. M., Herrnstein, J. R., and Galle, E. 2005, *ApJ* 624, 103
 Greenhill, L. J., Henkel, C., Becker, R., Wilson, T. L., and Wouterloot, J. G. A. 1995a, *A&A* 304, 21
 Greenhill, L. J., Jiang, D. R., Moran, J. M., Reid, M. J., Lo, K. Y., and Claussen, M. J. 1995b, *ApJ* 440, 619
 Greenhill, L. J., Moran, J. M., Herrnstein, J. R. 1997, *ApJ*, 481, L23
 Gruber, D. E., Matteson, J. L., Peterson, L. E., & Jung, G. V. 1999, *ApJ*, 520, 124
 Guainazzi, M., Mihara, T., Otani, C., Matsuoka, M., 1996, *PASJ*, 48, 781-799
 Herrnstein, J. R. et al. 1999, *Nature* 400, 539
 Ho, L. C., Filippenko, A. V., & Sargent, W. L. W. 1997, *ApJ* 112, 315
 Itoh, T. et al. 2008, *PASJ*, 60, S251-S261
 Ishisaki, Y., et. al. 2007, *PASJ*, 59, S113
 Kokubun M. et al. 2007, *PASJ*, 59, S53
 Koyama K. et al. 2007, *PASJ*, 59, S23
 Koyama K., Inoue, H., Tanaka, Y., Awaki, H., Takano, S., Ohashi, T., Matsuoka, M. 1989, *PASJ*, 41, 731-777
 Lasota, J.-P., Abramowicz, M. A., Chen, X., Krolik, J., Narayan, R., Yi, I. 1996 *ApJ*, 462, 142L
 Madejski, G., Done, C., Zycki, P. T., Greenhill, L. 2006 *ApJ*, 636, 72-82
 Madejski, G., Zycki, P., Done, C., Valinia, A., Blanco, P., Rothschild, R., Turek, B. 2000 *ApJ*, 535, L87-L90
 Makishima, K. et al. 1994, *PASJ* 46, L77
 Makishima, K. et al. 1989, *PASJ* 41, 697-708
 Makishima, K. et al. 2008, *PASJ* 60, 585-604
 Matt, G., Fabian, A. C., Guainazzi, M., Iwasawa, K., Bassani, L., Malaguti, G. 2000, *MNRAS*, 318, 173-179
 Miyoshi, M., Moran, J., Herrnstein, J., Greenhill, L., Nakai, N., Diamond, P., Inoue, M. 1995 *Nature* 373, 12
 Markowitz, A et al. 2008, *PASJ*, 60, 277
 Marconi, A., Risaliti, G., Gilli, R., Hunt, L. K., Maiolino, R., Salvati, M. 2004 *MNRAS*, 351, 169
 Maiolino, R., Salvati, M., Bassani, L., Dadina, M., della Ceca, R., Matt, G., Risaliti, G., Zamorani, G. 1998, *A&A*, 338, 781-794
 Narayan, R. Yi, I., 1995, *ApJ*, 452, 710
 Pietsch, W. and Read, A. M., 2002, *A&A* 384, 793
 Reeves, J. N., 2007, *PASJ*, 59, 301-314
 Reynolds, C. S., Nowak, M. A., and Maloney, P. R. 2000, *ApJ* 540, 143
 Revnivtsev, M., Gilfanov, M., Sunyaev, R., Jahoda, K., Markwardt, C. 2003, *A&A*, 411, 329
 Shirai, H., 2008, *PASJ*, 60, S263-S276
 Sunyaev, R. A. & Trümper, J. 1979, *Nature*, 279, 506
 Tully, R. B. 1988, *Science*, 242, 310
 Tueller, J., Mushotzky, R. F., Barthelmy, S., Cannizzo, J. K., Gehrels, N., Markwardt, C. B., Skinner, G. K., Winter, L. M. 2008, *PASJ*, 60, 277
 Terashima, Y., Iyomoto, N., Ho, L. C., and Ptak, A. F., 2002, *ApJS* 139, 1
 Takahashi, T. et al. 2007, *PASJ*, 59, S35
 Ueda, Y. et al. 2007, *ApJL*, 664, L79
 Ueno, S., Koyama, K., Awaki, H., Hayashi, I., Blanco, Philip R., 1996, *PASJ*, 48, 389-394
 Warwick, R. S., Yaqoob, T., Pounds, K. A., Matsuoka, M., Yamauchi, Makoto 1989, *PASJ*, 41, 721-730
 Wilkes, B. J., Schmidt, G. D., Smith, P. S., Mathur, S., McLeod, K. K. 1995, *ApJ* L 455, L13+
 Wilson, A. S., Yang, Y., and Cecil, G., 2001, *ApJ* 560, 689
 Yang, Y., Li, B., Wilson, A. S., Reynolds, C. S. 2007, *ApJ*, 660, 1106-1117
 Yaqoob, T., Y. 1992, *MNRAS*, 258 198-216